ELSEVIER

Journal of Fluids and Structures 20 (2005) 1105–1125

JOURNAL OF FLUIDS AND STRUCTURES

www.elsevier.com/locate/jfs

Fully coupled fluid–structural interactions using an efficient high resolution upwind scheme

X.-Y. Chen, G.-C. Zha*

Department of Mechanical and Aerospace Engineering, University of Miami, Coral Gables, Florida 33124, USA

Received 29 April 2004; accepted 24 February 2005
Available online 14 June 2005

Abstract

The E-CUSP upwind scheme recently developed by Zha and Hu is extended to the moving grid system and is applied to calculate the flow-induced vibration based on a fully coupled fluid–structure interaction methodology. The scheme is used to calculate the flow-induced vibration of an elastically mounted cylinder, forced pitching airfoil, and an elastically mounted airfoil. The numerical results are compared with experimental data and have demonstrated the accuracy, efficiency and robustness of the new E-CUSP scheme for solving flow-induced vibration problems with moving mesh systems.

Keywords: Flow induced vibration; Flutter; Fluid-structural interaction; Low diffusion upwind scheme

1. Introduction

Flow-induced structural vibration is one of the most critical technical problems affecting the reliability, cost and safety of aircraft. For a certain class of flow–structure problems, e.g. those involving separated flows or large structural deformations, there is a lack of efficient and highly accurate computational tools to study the basic physics and predict the structural failure. This is due to the very complicated nonlinear flow–structure interaction and multidisciplinary (fluid and structure) requirements. The problems exist in both the airframe and aircraft engine systems.

There are generally two types of methods used to calculate the fluid–structure interaction problems in the time domain; in these methods, the fluid and structure governing equations are loosely coupled or fully coupled. In a loosely coupled model the structural response lags behind the flow field solution. This type of method may be limited to first-order accuracy in time, regardless of the temporal accuracy of the individual solvers (Melville and Morton, 1998). In the fully coupled model, the flow field and structure always respond simultaneously by exchanging the aerodynamic forcing and structural displacement within each iteration. Obviously, only the fully coupled model is rigorous in the physical sense.

Recently, efforts have been made to develop prediction capabilities for flow-induced vibration. Bendiksen and Kousen (1987) pioneered the research by using an explicit CFD code coupled with a structural integrator based on the convolution integral to obtain the flutter boundary for a NACA 64A010 airfoil. The loosely coupled model between the fluid and structural solvers is included in the work conducted by Guruswamy (1990), Lee-Rausch and Batina (1996),

*Corresponding author.
E-mail address: zha@apollo.eng.miami.edu (G.-C. Zha).

0889-9746/$ - see front matter
doi:10.1016/j.jfluidstructs.2005.02.011

Smith (1989), Vermeersch et al. (1997), Darracq et al. (1998), Blom and Leyland (1997), Prananta et al. (1998), and Bohbot and Darracq (2001). Alonso and Jameson (1994) developed a model which is close to the fully coupled method with the structural displacement updated every several fluid solver iterations. The implicit Runge–Kutta method with multigrid acceleration is employed for the flow solver in Alonso's work (Alonso and Jameson, 1994; Alonso et al., 1995). In 1997–98, Morton et al. (1997), Melville et al. (1997), and Melville and Morton (1998) developed an implicit fully coupled fluid–structural interaction model, which used the Beam-Warming implicit scheme for the flow solver, coupled with a model structural solver. Liu et al. (2000) developed a fully coupled method using Jameson's explicit scheme with multigrid method and a finite element structural model.

Chen et al. (2004) have recently developed a fully coupled methodology for calculating the flow-induced vibrations. In their method, the Roe scheme is extended to the moving grid system and is used with the finite-volume method. Unlike the central differencing used in (Morton et al., 1997; Melville et al., 1997; Melville and Morton, 1998), the artificial dissipation does not need to be adjusted. The structural response is sensitive to different artificial dissipations. The unsteady solutions march in time by using a dual-time stepping implicit unfactored Gauss–Seidel iteration. The unsteady Navier–Stokes equations and the linear structural equations are fully coupled implicitly via successive iteration with pseudo-time stepping. The moving/deforming mesh strategy is based on two mesh zones: a fine mesh zone surrounding the solid body without mesh deformation, and a coarse mesh zone surrounding the fine mesh zone and deforming with the solid object motion. This mesh deformation strategy can maintain the orthogonality of the mesh near the wall and save CPU time spent to remesh the grid near the solid wall.

However, the calculation based on a fully coupled fluid–structure interaction is CPU-expensive due to the intensive iterations between the fluid system and structure system. Hence, a numerical scheme that is CPU-efficient and accurate is very desirable. The Roe scheme used in Chen et al. (2004) for the flow field calculation consumes a lot of CPU time, due to its matrix operation for the numerical dissipation. The theory and methodology introduced here (Chen et al., 2004) will employ a more CPU-efficient scheme by avoiding the dissipation matrix to calculate the flow-induced vibrations.

Recently, there have been many efforts to develop efficient Riemann solvers using scalar dissipation instead of matrix dissipation. For the scalar dissipation Riemann solver schemes, there are generally two types: H-CUSP schemes and E-CUSP schemes (Jameson, 1993, 1995a,b). The abbreviation CUSP stands for "convective upwind and split pressure", named by Jameson (1993, 1995a,b). The H-CUSP schemes have the total enthalpy from the energy equation in their convective vector, while the E-CUSP schemes use the total energy in the convective vector. Liou's AUSM family schemes (Liou, 1996), Van Leer-Hänel scheme (Hänel et al., 1987), and Edwards's LDFSS schemes (Edwards, 1995, 1997) belong to the H-CUSP group.

The H-CUSP schemes may have the advantage of better conserving the total enthalpy for steady state flows. However, from the characteristic theory point of view, the H-CUSP schemes are not fully consistent with the disturbance propagation directions, which may affect the stability and robustness of the schemes (Zha and Hu, 2004). The H-CUSP scheme may have more inconsistencies when it is extended to the moving grid system. It will leave the pressure term multiplied by the grid velocity in the energy flux, which cannot be contained in the total enthalpy, and must therefore be treated as part of the pressure term. From a characteristic point of view, it is not obvious how to treat this term in a consistent manner.

Recently, Zha and Hu (2004) suggested an efficient E-CUSP scheme which is consistent with the characteristic directions. The scheme has low diffusion and is able to capture crisp shock profiles and exact contact discontinuities. The scheme is more CPU-efficient since it only uses scalar dissipation. In addition, it is fairly straightforward to extend the E-CUSP scheme of Zha–Hu to the moving grid system. This is because the grid velocity belongs to the convective terms in the E-CUSP schemes. The pressure term is determined by the weighted average based on the wave eigenvalues from downstream and upstream. The Zha–Hu scheme is more efficient than the Roe scheme without matrix operation. For a 2-D nozzle calculation, the CPU time to evaluate the flux using the Zha–Hu scheme is only about one-quarter of that needed by the Roe scheme (Zha and Hu, 2004). The Zha–Hu E-CUSP scheme is further modified to remove the temperature oscillations occurring occasionally near the computational boundary (Zha, 2004).

The objective of the current study is to apply the newly suggested E-CUSP scheme of Zha–Hu to a fully coupled fluid–structure interaction to achieve high efficiency and accuracy. No temperature oscillations are observed in all the results of the present calculation, and hence the modified scheme suggested by Zha (2004) is not used. The above methodology is proved to be robust, accurate and efficient by the computed flow-induced vibration of an elastically mounted cylinder, a transonic pitching airfoil, and the elastically mounted NACA 64A010 airfoil.

2. CFD aerodynamic model

2.1. Flow governing equations

The governing equations for the flow field computation are the Reynolds-Averaged Navier–Stokes equations (RANS) with Favre mass average which can be transformed to the generalized coordinates and expressed as

$$\frac{\partial \mathbf{Q}'}{\partial t}+\frac{\partial \mathbf{E}'}{\partial \xi}+\frac{\partial \mathbf{F}'}{\partial \eta}+\frac{\partial \mathbf{G}'}{\partial \zeta}=\frac{1}{\mathrm{Re}}\left(\frac{\partial \mathbf{E}'_v}{\partial \xi}+\frac{\partial \mathbf{F}'_v}{\partial \eta}+\frac{\partial \mathbf{G}'_v}{\partial \zeta}\right), \tag{1}$$

where Re is the Reynolds number, and

$$\mathbf{Q}'=\frac{\mathbf{Q}}{J}, \tag{2}$$

$$\mathbf{E}'=\frac{1}{J}(\xi_t\mathbf{Q}+\xi_x\mathbf{E}+\xi_y\mathbf{F}+\xi_z\mathbf{G})=\frac{1}{J}(\xi_t\mathbf{Q}+\mathbf{E}''), \tag{3}$$

$$\mathbf{F}'=\frac{1}{J}(\eta_t\mathbf{Q}+\eta_x\mathbf{E}+\eta_y\mathbf{F}+\eta_z\mathbf{G})=\frac{1}{J}(\eta_t\mathbf{Q}+\mathbf{F}''), \tag{4}$$

$$\mathbf{G}'=\frac{1}{J}(\zeta_t\mathbf{Q}+\zeta_x\mathbf{E}+\zeta_y\mathbf{F}+\zeta_z\mathbf{G})=\frac{1}{J}(\zeta_t\mathbf{Q}+\mathbf{G}''), \tag{5}$$

$$\mathbf{E}'_v=\frac{1}{J}(\xi_x\mathbf{E}_v+\xi_y\mathbf{F}_v+\xi_z\mathbf{G}_v), \tag{6}$$

$$\mathbf{F}'_v=\frac{1}{J}(\eta_x\mathbf{E}_v+\eta_y\mathbf{F}_v+\eta_z\mathbf{G}_v), \tag{7}$$

$$\mathbf{G}'_v=\frac{1}{J}(\zeta_x\mathbf{E}_v+\zeta_y\mathbf{F}_v+\zeta_z\mathbf{G}_v), \tag{8}$$

in which J is the transformation Jacobian. The variable vector $\mathbf{Q}$, and inviscid flux vectors $\mathbf{E}$, $\mathbf{F}$, and $\mathbf{G}$ are

$$\mathbf{Q}=\begin{pmatrix}\bar\rho\\ \bar\rho\tilde u\\ \bar\rho\tilde v\\ \bar\rho\tilde w\\ \bar\rho\tilde e\end{pmatrix},\quad \mathbf{E}=\begin{pmatrix}\bar\rho\tilde u\\ \bar\rho\tilde u\tilde u+\tilde p\\ \bar\rho\tilde u\tilde v\\ \bar\rho\tilde u\tilde w\\ (\bar\rho\tilde e+\tilde p)\tilde u\end{pmatrix},\quad \mathbf{F}=\begin{pmatrix}\bar\rho\tilde v\\ \bar\rho\tilde u\tilde v\\ \bar\rho\tilde v\tilde v+\tilde p\\ \bar\rho\tilde w\tilde v\\ (\bar\rho\tilde e+\tilde p)\tilde v\end{pmatrix},\quad \mathbf{G}=\begin{pmatrix}\bar\rho w\\ \bar\rho\tilde u\tilde w\\ \bar\rho\tilde v\tilde w\\ \bar\rho\tilde w\tilde w+\tilde p\\ (\bar\rho\tilde e+\tilde p)\tilde w\end{pmatrix},$$

where $\mathbf{E}''$, $\mathbf{F}''$, and $\mathbf{G}''$ are the inviscid fluxes at the stationary grid system and are expressed as

$$\mathbf{E}''=\xi_x\mathbf{E}+\xi_y\mathbf{F}+\xi_z\mathbf{G},$$

$$\mathbf{F}''=\eta_x\mathbf{E}+\eta_y\mathbf{F}+\eta_z\mathbf{G},$$

$$\mathbf{G}''=\zeta_x\mathbf{E}+\zeta_y\mathbf{F}+\zeta_z\mathbf{G};$$

the viscous flux vectors are given by

$$\mathbf{E}_v=\begin{pmatrix}0\\ \bar\tau_{xx}-\overline{\rho u''u''}\\ \bar\tau_{xy}-\overline{\rho u''v''}\\ \bar\tau_{xz}-\overline{\rho u''w''}\\ Q_x\end{pmatrix},\quad \mathbf{F}_v=\begin{pmatrix}0\\ \bar\tau_{yx}-\overline{\rho v''u''}\\ \bar\tau_{yy}-\overline{\rho v''v''}\\ \bar\tau_{yz}-\overline{\rho v''w''}\\ Q_y\end{pmatrix},\quad \mathbf{G}_v=\begin{pmatrix}0\\ \bar\tau_{zx}-\overline{\rho w''u''}\\ \bar\tau_{zy}-\overline{\rho w''v''}\\ \bar\tau_{zz}-\overline{\rho w''w''}\\ Q_z\end{pmatrix}.$$

In the above equations, ρ is the density, u, v, and w are the Cartesian velocity components in the x, y and z directions, p is the static pressure, and e is the total energy per unit mass. The overbar denotes the Reynolds-averaged quantity, and the tilde and double-prime denote the Favre mean and Favre fluctuating part of the turbulent motion, respectively. All

the flow variables in the above equations are nondimensionlized by using the freestream quantities and a reference length L.

Let subscript 1, 2 and 3 represent the coordinates, x, y, and z, and use the Einstein summation convention. The shear-stress and Q_x, Q_y, Q_z terms in nondimensional form can be expressed in tensor form as

$$\tilde{\tau}_{ij} = -\frac{2}{3}\tilde{\mu}\frac{\partial \tilde{u}_k}{\partial x_k}\delta_{ij} + \tilde{\mu}\left(\frac{\partial \tilde{u}_i}{\partial x_j} + \frac{\partial \tilde{u}_j}{\partial x_i}\right), \tag{9}$$

$$Q_i = \tilde{u}_j(\tilde{\tau}_{ij} - \overline{\rho u_i'' u_j''}) - (\tilde{q}_i + C_p\overline{\rho T'' u_i''}), \tag{10}$$

where the mean molecular heat flux is

$$\tilde{q}_i = -\frac{\tilde{\mu}}{(\gamma-1)\,\mathrm{Pr}}\frac{\partial a^2}{\partial x_i}. \tag{11}$$

The molecular viscosity $\tilde{\mu} = \tilde{\mu}(\tilde{T})$ is determined by the Sutherland law, and $a = \sqrt{\gamma RT_\infty}$ is the speed of sound. The equation of state closes the system,

$$\bar{\rho}\tilde{e} = \frac{\tilde{p}}{(\gamma-1)} + \frac{1}{2}\bar{\rho}(\tilde{u}^2 + \tilde{v}^2 + \tilde{w}^2) + \kappa, \tag{12}$$

where γ is the ratio of specific heats, and κ is the Favre mass-averaged turbulence kinetic energy. The turbulent shear stress and heat flux appearing in the above equations are calculated using the Baldwin–Lomax model (Baldwin and Lomax, 1978).

It was pointed out by Thomas and Lombard (1979) that, due to the mixed temporal and spatial derivatives after discretization, an additional term appears, which theoretically equals zero, but numerically still remains. Consequently, numerical error could be introduced in the discretized form of the equations of the flow motion if this term is neglected. In order to reduce or avoid this error, the geometric conservation law needs to be enforced. In other words, the following additional term should be added to the right-hand side of the equations as a source term:

$$\mathbf{S} = \mathbf{Q}\left[\frac{\partial J^{-1}}{\partial t} + \left(\frac{\xi_t}{J}\right)_\xi + \left(\frac{\eta_t}{J}\right)_\eta + \left(\frac{\zeta_t}{J}\right)_\zeta\right]. \tag{13}$$

To implement this option in the flow solver, the source term is then linearized, such that

$$\mathbf{S}^{n+1} = \mathbf{S}^n + \frac{\partial \mathbf{S}}{\partial \mathbf{Q}}\Delta\mathbf{Q}^{n+1}. \tag{14}$$

2.2. Time marching scheme

The time-dependent governing equation (1) is solved using the control volume method with the concept of dual time stepping suggested by Jameson (1991). A pseudo-temporal term $\partial\mathbf{Q}/\partial\tau$ is added to the governing equation (1). This term vanishes at the end of each physical time step and has no influence on the accuracy of the solution. However, instead of using the explicit scheme as in Jameson (1991), an implicit pseudo time marching scheme using Gauss–Seidel iteration is employed to achieve high CPU efficiency. The implicit Gauss–Seidel iteration will allow a much larger CFL number for both physical time step and pseudo-time step to accelerate the convergence within each physical time step. The other advantage of the dual time approach is its easy implementation of implicit parallel computation of unsteady flow. Using the pseudo time step, the information exchange on the domain partition boundary can be treated in the same way as steady-state calculation. When the solution has converged within each physical time step for parallel computation, the time accurate information is exchanged through the domain partition boundary.

For unsteady time accurate computations, the temporal term is discretized implicitly using a three point, backward differencing as the following:

$$\frac{\partial \mathbf{Q}}{\partial t} = \frac{3Q^{n+1} - 4Q^n + Q^{n-1}}{2\Delta t}, \tag{15}$$

where n is the time level index. The pseudo temporal term is discretized with first-order Euler scheme. Let m stand for the iteration index within a physical time step. The semi-discretized governing equation (1) can

then be expressed as

$$\left[\left(\frac{1}{\Delta\tau}+\frac{1.5}{\Delta t}\right)I-\left(\frac{\partial R}{\partial Q}\right)^{n+1,m}\right]\delta Q^{n+1,m+1}=R^{n+1,m}-\frac{3Q^{n+1,m}-4Q^{n}+Q^{n-1}}{2\Delta t}, \tag{16}$$

where $\Delta\tau$ is the pseudotime step. The net flux going through the control volume, R, can be expressed by

$$R=-\frac{1}{V}\int_{s}[(F-F_v)\mathbf{i}+(G-G_v)\mathbf{j}+(H-H_v)\mathbf{k}]\cdot d\mathbf{s}, \tag{17}$$

where V is the volume of the control volume and $\mathbf{s}$ is the control volume surface area vector. Eq. (16) is solved using the unfactored Gauss–Seidel iteration. The method is unconditionally stable and can reach a very large pseudo time step since no factorization error is introduced.

2.3. The Zha–Hu E-CUSP scheme on a moving grid system

To clearly describe the formulations, the vectors $\mathbf{Q}$ and $\mathbf{E}'$ in Eq. (3) are given below:

$$\mathbf{Q}=\begin{pmatrix}\bar{\rho}\\ \bar{\rho}\tilde{u}\\ \bar{\rho}\tilde{v}\\ \bar{\rho}\tilde{w}\\ \bar{\rho}\tilde{e}\end{pmatrix},\quad \mathbf{E}'=\frac{1}{J}\hat{\mathbf{E}},\quad \hat{\mathbf{E}}=\begin{pmatrix}\bar{\rho}\tilde{U}\\ \bar{\rho}\tilde{u}\tilde{U}+\xi_x\tilde{p}\\ \bar{\rho}\tilde{v}\tilde{U}+\xi_y\tilde{p}\\ \bar{\rho}\tilde{w}\tilde{U}+\xi_z\tilde{p}\\ \bar{\rho}\tilde{e}\tilde{U}+\tilde{p}\bar{U}\end{pmatrix}. \tag{18}$$

$\tilde{U}$ is the contravariant velocity in ξ direction and is defined by

$$\tilde{U}=\xi_t+\xi_x\tilde{u}+\xi_y\tilde{v}+\xi_z\tilde{w}, \tag{19}$$

and $\bar{U}$ is defined as

$$\bar{U}=\tilde{U}-\xi_t. \tag{20}$$

The Jacobian matrix $\hat{\mathbf{A}}$ is defined as

$$\hat{\mathbf{A}}=\frac{\partial\hat{\mathbf{E}}}{\partial\mathbf{Q}}=\hat{\mathbf{T}}\hat{\mathbf{\Lambda}}\hat{\mathbf{T}}^{-1}, \tag{21}$$

where $\hat{\mathbf{T}}$ is the right eigenvector matrix of $\hat{\mathbf{A}}$, and $\hat{\mathbf{\Lambda}}$ is the eigenvalue matrix of $\hat{\mathbf{A}}$ on the moving grid system, with eigenvalues

$$(\tilde{U}+\tilde{C},\tilde{U}-\tilde{C},\tilde{U},\tilde{U},\tilde{U}), \tag{22}$$

where $\tilde{C}$ is the speed of sound, corresponding to the contravariant velocity

$$\tilde{C}=c\sqrt{\xi_x^2+\xi_y^2+\xi_z^2}, \tag{23}$$

and where $c=\sqrt{\gamma RT}$ is the physical speed of sound.

Due to the homogeneous relationship between $\mathbf{Q}$ and $\hat{\mathbf{E}}$, the following formulation applies:

$$\hat{\mathbf{E}}=\hat{\mathbf{A}}\mathbf{Q}=\hat{\mathbf{T}}\hat{\mathbf{\Lambda}}\hat{\mathbf{T}}^{-1}\mathbf{Q}. \tag{24}$$

In an E-CUSP scheme, the eigenvalue matrix is split as follows:

$$\hat{\mathbf{\Lambda}}=\begin{pmatrix}\tilde{U}-\tilde{C}&0&0&0&0\\ 0&\tilde{U}&0&0&0\\ 0&0&\tilde{U}&0&0\\ 0&0&0&\tilde{U}&0\\ 0&0&0&0&\tilde{U}+\tilde{C}\end{pmatrix}=\tilde{U}[\mathbf{I}]+\begin{pmatrix}-\tilde{C}&0&0&0&0\\ 0&0&0&0&0\\ 0&0&0&0&0\\ 0&0&0&0&0\\ 0&0&0&0&\tilde{C}\end{pmatrix}. \tag{25}$$

The grid velocity term $\xi_t[\mathbf{I}]$ due to the moving mesh is naturally included in the convective term, $\tilde{U}$, as given in Eq. (19). Therefore, Eq. (24) becomes

$$\hat{\mathbf{E}} = \hat{\mathbf{T}}\left\{\tilde{U}[\mathbf{I}] + \begin{pmatrix} -\tilde{C} & 0 & 0 & 0 & 0 \\ 0 & 0 & 0 & 0 & 0 \\ 0 & 0 & 0 & 0 & 0 \\ 0 & 0 & 0 & 0 & 0 \\ 0 & 0 & 0 & 0 & \tilde{C} \end{pmatrix}\right\}\hat{\mathbf{T}}^{-1}\mathbf{Q} = \hat{\mathbf{E}}^c + \hat{\mathbf{E}}^p = \begin{pmatrix} \bar{\rho}\tilde{U} \\ \bar{\rho}\tilde{u}\tilde{U} \\ \bar{\rho}\tilde{v}\tilde{U} \\ \bar{\rho}\tilde{w}\tilde{U} \\ \bar{\rho}\tilde{e}\tilde{U} \end{pmatrix} + \begin{pmatrix} 0 \\ \xi_x\tilde{p} \\ \xi_y\tilde{p} \\ \xi_z\tilde{p} \\ \tilde{p}\bar{U} \end{pmatrix}, \tag{26}$$

where $\hat{\mathbf{E}}^c$ and $\hat{\mathbf{E}}^p$ are namely the convective and pressure fluxes. As shown above, the way of splitting the total flux into convective and pressure fluxes in an E-CUSP scheme is purely based on the analysis of characteristics of the system. As shown in Eq. (26), the convective flux has the upwind characteristic $\tilde{U}$ and is only associated with the convective velocity. The pressure flux has a downwind and an upwind characteristic and it completely depends on the propagation of an acoustic wave.

The E-CUSP scheme of Zha–Hu (Zha and Hu, 2004) can be extended to a moving mesh system by the following:

$$\hat{\mathbf{E}}_{\frac{1}{2}} = \frac{1}{2}[(\bar{\rho}\tilde{U})_{\frac{1}{2}}(\mathbf{q}^c_L + \mathbf{q}^c_R) - |\bar{\rho}\tilde{U}|_{\frac{1}{2}}(\mathbf{q}^c_R - \mathbf{q}^c_L)] + \begin{pmatrix} 0 \\ P^+ p\tilde{\xi}_x \\ P^+\tilde{p}\xi_y \\ P^+\tilde{p}\xi_z \\ \frac{1}{2}\tilde{p}(\bar{U} + \bar{C}_{\frac{1}{2}}) \end{pmatrix}_L + \begin{pmatrix} 0 \\ P^-\tilde{p}\xi_x \\ P^-\tilde{p}\xi_y \\ P^-\tilde{p}\xi_z \\ \frac{1}{2}\tilde{p}(\bar{U} - \bar{C}_{\frac{1}{2}}) \end{pmatrix}_R, \tag{27}$$

where

$$(\bar{\rho}\tilde{U})_{\frac{1}{2}} = (\bar{\rho}_L\tilde{U}^+_L + \bar{\rho}_R\tilde{U}^-_R), \tag{28}$$

$$\mathbf{q}^c = \begin{pmatrix} 1 \\ \tilde{u} \\ \tilde{v} \\ \tilde{w} \\ \tilde{e} \end{pmatrix}, \tag{29}$$

$$\tilde{C}_{\frac{1}{2}} = \tfrac{1}{2}(\tilde{C}_L + \tilde{C}_R), \tag{30}$$

$$\tilde{M}_L = \frac{\tilde{U}_L}{\tilde{C}_{\frac{1}{2}}}, \quad \tilde{M}_R = \frac{\tilde{U}_R}{\tilde{C}_{\frac{1}{2}}}, \tag{31}$$

$$\tilde{U}^+_L = \tilde{C}_{\frac{1}{2}}\left\{\frac{\tilde{M}_L + |\tilde{M}_L|}{2} + \alpha_L\left[\frac{1}{4}(\tilde{M}_L + 1)^2 - \frac{\tilde{M}_L + |\tilde{M}_L|}{2}\right]\right\}, \tag{32}$$

$$\tilde{U}^-_R = \tilde{C}_{\frac{1}{2}}\left\{\frac{\tilde{M}_R - |\tilde{M}_R|}{2} + \alpha_R\left[-\frac{1}{4}(\tilde{M}_R - 1)^2 - \frac{\tilde{M}_R - |\tilde{M}_R|}{2}\right]\right\}, \tag{33}$$

$$\alpha_L = \frac{2(\tilde{p}/\bar{\rho})_L}{(\tilde{p}/\bar{\rho})_L + (\tilde{p}/\bar{\rho})_R}, \quad \alpha_R = \frac{2(\tilde{p}/\bar{\rho})_R}{(\tilde{p}/\bar{\rho})_L + (\tilde{p}/\bar{\rho})_R}, \tag{34}$$

$$P^{\pm} = \tfrac{1}{4}(\tilde{M} \pm 1)^2(2 \mp \tilde{M}) \pm \alpha\tilde{M}(\tilde{M}^2 - 1)^2, \quad \alpha = \tfrac{3}{16}, \tag{35}$$

$$\bar{C} = \tilde{C} - \xi_t, \tag{36}$$

$$\bar{C}_{\frac{1}{2}} = \tfrac{1}{2}(\bar{C}_L + \bar{C}_R). \tag{37}$$

Please note that, in the energy equation of the pressure splitting, $\bar{U}$ and $\bar{C}$ are used instead of $\tilde{U}$ and $\tilde{C}$. The term $\bar{C}$ is constructed by taking into account the effect of the grid velocity so that the flux will transist from subsonic to supersonic smoothly. When $\xi_t = 0$, Eq. (27) naturally returns to the one for a stationary grid.

For supersonic flow, when $\tilde{U}_L \geqslant \tilde{C}$, then $\hat{\mathbf{E}}_{\frac{1}{2}} = \hat{\mathbf{E}}_L$, and when $\tilde{U}_R \leqslant -\tilde{C}$, $\hat{\mathbf{E}}_{\frac{1}{2}} = \hat{\mathbf{E}}_R$.

2.4. Boundary conditions

The flow field is solved subject to appropriate boundary conditions described below.

(i) *Upstream boundary condition*. The outer boundary is divided into upstream and downstream boundaries according to whether the direction of its segment is toward or backward to the ambient flow direction. On the upstream boundary, it is assumed that the streamwise velocity u is uniform, and transverse velocity $v = 0$. Other primitive variables are specified according to the freestream condition, except the pressure term, which is extrapolated from the interior.

(ii) *Downstream boundary condition*. All the flow quantities are extrapolated from the interior, except for pressure, which is set to be its freestream value.

(iii) *Solid wall boundary condition*. At a moving boundary surface, the no-slip condition is enforced by extrapolating the velocity between the phantom and interior cells,

$$u_0 = 2u_b - u_1, \quad v_0 = 2v_b - v_1, \tag{38}$$

where u_0 and v_0 denote the velocity at a phantom cell, u_1 and v_1 denote the velocity at the first interior cell close to the boundary, and $u_b = \dot{x}_b$ and $v_b = \dot{y}_b$ denote the velocity of the moving boundary.

The other two conditions to be imposed on the solid wall are the adiabatic wall condition and the inviscid normal momentum equation (Morton et al., 1997). These are given by the following:

$$\frac{\partial T}{\partial \eta} = 0, \quad \frac{\partial p}{\partial \eta} = -\left(\frac{\rho}{\eta_x^2 + \eta_y^2}\right)(\eta_x \ddot{x}_b + \eta_y \ddot{y}_b). \tag{39}$$

3. Structural models

3.1. Elastically mounted cylinder

For the computations on the vortex-induced oscillations of a cylinder, which is elastically supported, as shown in Fig. 1, so that it oscillates only in the direction aligned with or normal to the incoming flow, the structural dynamic equations which governs the motion of the cylinder are

$$m\ddot{x} + C_x\dot{x} + K_x x = D_f, \tag{40}$$

$$m\ddot{y} + C_y\dot{y} + K_y y = L_f. \tag{41}$$

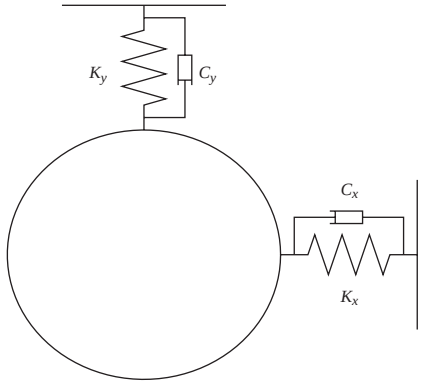

Fig. 1. Sketch of the elastically mounted cylinder.

These equations are solved implicitly, together with the equations of flow motion, Eq. (16), in a fully coupled manner. In Eq. (40), $\ddot{x}$, $\dot{x}$, and x represent the dimensionless horizontal acceleration, velocity and displacement of the moving cylinder, respectively. Similarly, $\ddot{y}$, $\dot{y}$, and y in Eq. (41) represent the acceleration, velocity and displacement in the vertical direction. The terms m, L_f, and D_f are the mass, lift, and drag per unit span, respectively, C_x and C_y are the damping coefficients in horizontal and vertical directions, and K_x and K_y are the spring constants in horizontal and vertical directions. In the present study, this 'self-excited oscillators' is assumed to have the same response in both directions, i.e. $C_x = C_y$ and $K_x = K_y$.

If the normalization procedure is applied to Eqs. (40) and (41) by using the same reference scales of those used for the equations of flow motion, the following nondimensional equations are obtained:

$$\ddot{x} + 2\zeta\left(\frac{2}{\bar{u}}\right)\dot{x} + \left(\frac{2}{\bar{u}}\right)^2 x = \frac{2}{\mu_s \pi} C_d, \tag{42}$$

$$\ddot{y} + 2\zeta\left(\frac{2}{\bar{u}}\right)\dot{y} + \left(\frac{2}{\bar{u}}\right)^2 y = \frac{2}{\mu_s \pi} C_l, \tag{43}$$

where ζ is the nondimensional structural damping coefficient calculated by $\zeta = C_{x,y}/[2(mK_{x,y})^{1/2}]$, $\bar{u}$ is the reduced velocity defined by $\bar{u} = U_\infty/b\omega$, b is radius of the cylinder, $\omega = (K_{x,y}/m)^{1/2}$, the mass ratio defined by $\mu_s = m/\pi\rho_\infty b^2$, and C_d and C_l are the drag and lift force coefficients respectively. Then the equations are transformed to a matrix form and expressed by

$$[\mathbf{M}]\frac{\partial\{\mathbf{S}\}}{\partial t} + [\mathbf{K}]\{\mathbf{S}\} = \mathbf{q}, \tag{44}$$

where

$$\mathbf{S} = \begin{pmatrix} x \\ \dot{x} \\ y \\ \dot{y} \end{pmatrix}, \quad \mathbf{M} = [I], \quad \mathbf{K} = \begin{pmatrix} 0 & -1 & 0 & 0 \\ (2/\bar{u})^2 & 2\zeta(2/\bar{u}) & 0 & 0 \\ 0 & 0 & 0 & -1 \\ 0 & 0 & (2/\bar{u})^2 & 2\zeta(2/\bar{u}) \end{pmatrix}, \quad \mathbf{q} = \begin{pmatrix} 0 \\ (2/\mu_s\pi)C_d \\ 0 \\ (2/\mu_s\pi)C_l \end{pmatrix}.$$

To couple the structural equations with the equations of flow motion and solve them implicitly in each physical time step, the above equations are discretized and integrated in a manner consistent with Eq. (16) to yield

$$\left(\frac{1}{\Delta\tau}\mathbf{I} + \frac{1.5}{\Delta t}\mathbf{M} + \mathbf{K}\right)\delta S^{n+1,m+1} = -\mathbf{M}\frac{3\mathbf{S}^{n+1,m} - 4\mathbf{S}^n + \mathbf{S}^{n-1}}{2\Delta t} - \mathbf{K}\mathbf{S}^{n+1,m} + \mathbf{q}^{n+1,m+1}, \tag{45}$$

where n is the physical time level index and m stands for the pseudo-time index. The detailed coupling procedure between the fluid and structural systems is given in Section 4.

Giles (1995) shows that by using second-order backward differentiation to solve structural equations, $\omega_o\Delta t$ should be less than 0.1 to reduce the error to an acceptable range. In the present computations, about 100 time steps are used within one cycle for all the cases, and $\omega_o\Delta t$ is about 0.01 and lies in the acceptable range.

3.2. Elastically mounted airfoil

Unlike the structural model of the vortex-induced oscillating cylinder, the system of the elastically mounted airfoil is assumed to be undamped. The airfoil is allowed to move in pitch about a given elastic axis and plunge vertically. The pitch axis is defined by a distance a, which is the multiple of the semi-chord length with the origin point located at the mid-chord position. If a is positive, the axis is located downstream of the mid-chord. Conversely, if a is negative, the axis is located upstream of the mid-chord point.

A sketch of the elastically mounted airfoil is depicted in Fig. 2. The motion of such an elastic system can be described by using the following equations:

$$m\ddot{h} + S_\alpha\ddot{\alpha} + K_h h = -L_f, \tag{46}$$

$$S_\alpha\ddot{h} + I_\alpha\ddot{\alpha} + K_\alpha\alpha = M_f, \tag{47}$$

where h and α are the plunging and pitching displacements, respectively, m is the mass per unit span, S_α is the static moment around the elastic axis, I_α is the rotational moment of inertia, K_h and K_α are plunging and pitching spring

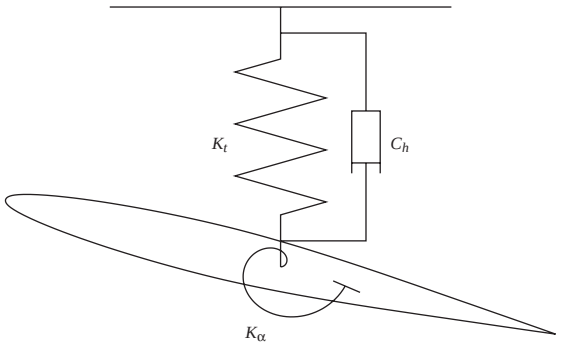

Fig. 2. Sketch of the elastically mounted airfoil.

constants, respectively, L_f is the lift force and M_f is the moment about the elastic axis. The equations of the structure motion (46) and (47) are normalized by using semi-chord b as the length dimension and the uncoupled natural frequency in pitch ω_α as the time scale. They are expressed as follows:

$$\ddot{h} + x_\alpha \ddot{\alpha} + \left(\frac{\omega_h}{\omega_\alpha}\right)^2 h = -\frac{U^{*2}}{\mu\pi} C_l, \tag{48}$$

$$x_\alpha \ddot{h} + r_\alpha^2 \ddot{\alpha} + r_\alpha^2 \alpha = \frac{U^{*2}}{\mu\pi} C_m, \tag{49}$$

where x_α is the static unbalance, ω_h is the uncoupled natural frequency in plunge, r_α^2 is the squared radius of gyration, U^* is the reduced velocity defined as $U_\infty/\omega_\alpha b$, and C_l and C_m are the lift and moment coefficients, respectively. Since the time scale used in Eqs. (48) and (49) is different from the one used in the governing equations of flow, the structural dimensionless time t_s^* needs to be rescaled and kept consistent within the entire system during the computation. More precisely, $t_s^* = \omega_\alpha L/U_\infty t_f^*$, where t_f^* is the dimensionless time and the L is the length scale for the flow field. Finally the equations are cast into the form of Eqs. (44) and (45), and the corresponding matrices are:

$$\mathbf{S} = \begin{pmatrix} h \\ \dot{h} \\ \alpha \\ \dot{\alpha} \end{pmatrix}, \quad \mathbf{M} = \begin{pmatrix} 1 & 0 & 0 & 0 \\ 0 & 1 & 0 & x_\alpha \\ 0 & 0 & 1 & 0 \\ 0 & x_\alpha & 0 & r_\alpha^2 \end{pmatrix}, \quad \mathbf{K} = \begin{pmatrix} 0 & -1 & 0 & 0 \\ (\omega_h/\omega_\alpha)^2 & 0 & 0 & 0 \\ 0 & 0 & 0 & -1 \\ 0 & 0 & r_\alpha^2 & 0 \end{pmatrix}, \quad \mathbf{q} = \begin{pmatrix} 0 \\ -(U^{*2}/\mu\pi)C_l \\ 0 \\ (U^{*2}/\mu\pi)C_m \end{pmatrix}.$$

4. Flow–structure coupling

Within a physical time step, the structural motion and flow field are unknown and need to be solved iteratively between the fluid and structural systems in a fully coupled manner. The following is the procedure.

(i) The variables at new time level $n+1$ of the flow and structural equations are initially set to be the values at time level n.

(ii) The aerodynamic forces including lift, drag, and torque exerting on the solid body of the object are calculated.

(iii) The position of the moving object subject to the aerodynamic forces is determined by solving the structural equations.

(iv) The mesh is regenerated and the grid velocity at each node point is calculated according to the updated structural position.

(v) The flow field is calculated by solving the equations of flow motion for the updated mesh and structural position.

(vi) The maximum residuals for both solutions of the flow and the structural equations are checked. If the maximum residuals are greater than the prescribed convergence criteria, step (ii) is repeated and the next pseudo-time level becomes $m+1$; otherwise, the flow field and movement of the object are determined and step (i) is repeated to start the next new physical time step $n+1$. The procedure can be also seen in the flow chart given in Fig. 3.

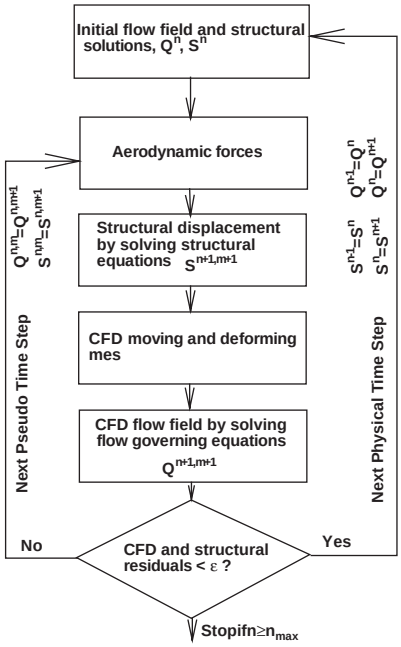

Fig. 3. Fully coupled fluid–structure interaction calculation procedure.

For moving-object computation, the mesh is designed in such a way that the fine mesh zone around the object moves rigidly with the object and the coarse mesh zone covers the rest of the computational domain by distorting its grids using an algebraic method. Consequently, the mesh refinement around the solid wall is the same throughout the simulation and the same grid quality (e.g. y^+) can be achieved in the boundary layer region regardless of the position of the object. Avoiding remeshing in the fine mesh zone also saves CPU time, since a set of differential equations are usually solved for the interior node points of the zone.

5. Results and discussion

Presented in this section are numerical results for the vortex-induced oscillation of a cylinder, the forced pitching of a NACA 64A010 airfoil, and the elastic response of a NACA 64A010 airfoil.

5.1. Elastically mounted cylinder

5.1.1. Stationary cylinder

The flow past a stationary cylinder is used as an unsteady flow validation case. The fine mesh zone mentioned in the previous section is shown in Fig. 4. The baseline mesh dimensions are 120×80 in the circumferential and radial directions. After intensive numerical experiments, the far-field boundary is chosen to be located 20 diameters away from the center of the cylinder because the solution is not sensitive to the far field boundary at this far-field range. The Reynolds number based on the free-stream condition and cylinder diameter is $\mathrm{Re} = 500$. The laminar Navier–Stokes equations are solved here for this low Reynolds number.

The computed drag and lift coefficients are shown in Fig. 5. As shown in the figure, the lift oscillates at a certain frequency in terms of the Strouhal number St_{C_l}. The drag coefficient oscillates with twice that frequency, St_{C_d}. The results of the mesh refinement study with the corresponding experimental and numerical results by other authors are listed in Table 1.

Table 1 shows that the predicted vortex shedding frequency based on the baseline mesh agrees fairly well with experiment (Roshko, 1954; Goldstein, 1938). When the mesh is refined, the results are shifted a little away from the experiment values, but have the same trend and range as the tabulated results of Alonso et al. (1995).

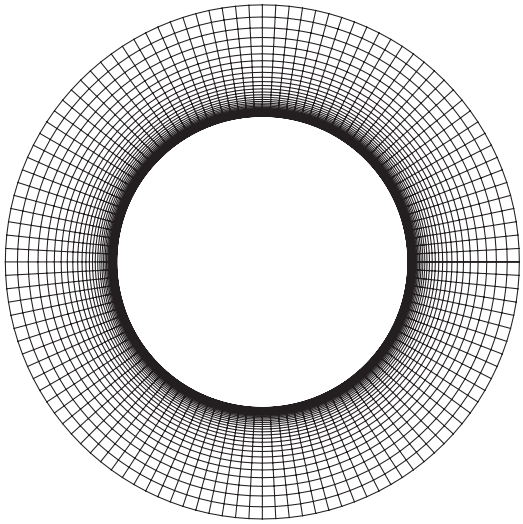

Fig. 4. The near-wall zone mesh around the solid surface of the cylinder.

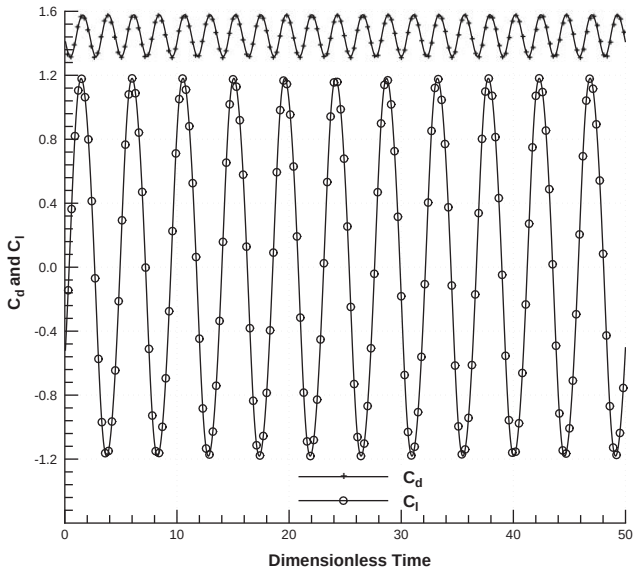

Fig. 5. Time histories of the lift and drag coefficients of the stationary cylinder due to vortex shedding.

Table 1
Results of mesh refinement study and comparison with the experiments

Mesh dimension	St_{C_d}	St_{C_l}	St_{C_m}	C_l	C_d
120×80	0.4395	0.2197	0.2197	± 1.1810	1.4529 ± 0.1305
200×120	0.4516	0.2246	0.2246	± 1.2267	1.4840 ± 0.1450
Roshko (1954)		0.2075			
Goldstein (1938)		0.2066			
384×96 Alonso et al. (1995)	0.46735	0.23313		1.14946($C_{l\max}$)	1.31523($C_{d\mathrm{avg}}$)

5.1.2. Vortex-induced oscillating cylinder

After validating the stationary cylinder vortex shedding flow, the cylinder is released to be controlled by the structure model as shown in Fig. 1. The corresponding structural equations are given in Section 3.1. Same as the stationary cylinder case, the laminar Navier–Stokes equations are used to solve the flow field with a low Reynolds number, $\mathrm{Re} = 500$.

Using the temporally periodic solution obtained in the computation of the stationary cylinder as the initial flow field, the computation proceeds after the cylinder is allowed to move in both streamwise and transverse directions. For the purpose of comparison with the experimental data of Griffin (1992), several different combinations of structural parameters are used in the computations.

Morton et al. (1997) suggested to use the reduced velocity $\bar{u} = 1/\pi\mathrm{St}$, such that the structural oscillator works under or near the resonance conditions. Therefore, any St equal or close to the vortex shedding Strouhal number computed from the stationary cylinder could be used to determine $\bar{u}$. For all the cases of an oscillating cylinder, St is set to be 0.2, corresponding to $\bar{u} = 1.5915$. Different mass ratios, μ_s, are used to test the different responses of the structural system. These are equal to $1.2732, 5.0$, and 12.7324, respectively. To match the wide range of the experimental data, the damping ratio, ζ, is chosen from the range 0.001–1.583.

The CFL number for the pseudo-time steps varies from case to case. For cases of large cylinder movement, smaller pseudo time steps are used to limit the displacement of the cylinder during each iteration to achieve numerical stability. For example, for the small displacement case with $\mu_s = 12.732$, $\zeta = 0.158$, the CFL of the pseudo time is 500; for the very large displacement case with $\mu_s = 1.273$, $\zeta = 0.0158$, the CFL number used is 5.

The iteration number within one physical time step varies from 20 to 100. Fig. 6 shows a typical iteration history within one physical time step. Both residuals of CFD and structural solvers are reduced to machine zero. The structure solver usually converges faster than the CFD solver.

Fig. 7 displays the computed vorticity contours around the oscillating cylinder. It shows how the vortices are shed at the moment when the cylinder bounds back toward its mean position in the y direction.

A typical trajectory of the center position of the moving cylinder is plotted in Fig. 8, which is similar to the results computed by Blackburn and Karniadakis (1993) and Alonso et al. (1995).

All the numerical results for present study are plotted in Fig. 9 for the three values of μ_s. Also plotted are the computations of Alonso et al. (1995) with $\mu_s = 5.0$, computations of Morton et al. (1997) with $\mu_s = 12.73$, and the experimental data of Griffin (1992). In the figure, the abscissa is the reduced damping with the form of $8\pi^2\mathrm{St}^2\zeta m/\rho D^2$ (Blackburn and Karniadakis, 1993), and the ordinate is the cross-flow displacement of motion normalized by the diameter of the cylinder. Overall, very good agreement is observed between the present results and the experimental results, especially for the case of $\mu_s = 1.2732$. The figure shows that the higher values of mass ratios ($\mu_s = 5.0$ and $\mu_s = 12.7324$) give less satisfactory results than those with $\mu_s = 1.2732$, particularly at low damping ratios. However, they agree well with the results of Morton et al. (1997) ($\mu_s = 12.73$). It is worth mentioning that flow conditions used by

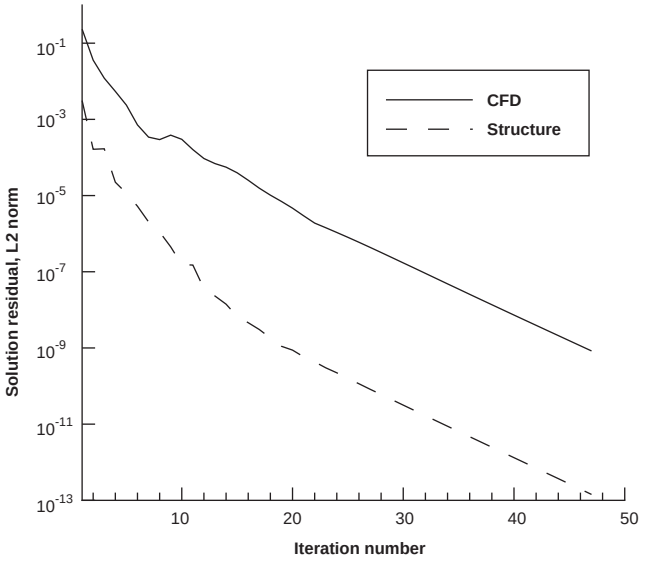

Fig. 6. Typical convergence histories of the CFD and structural solvers within one physical time step.

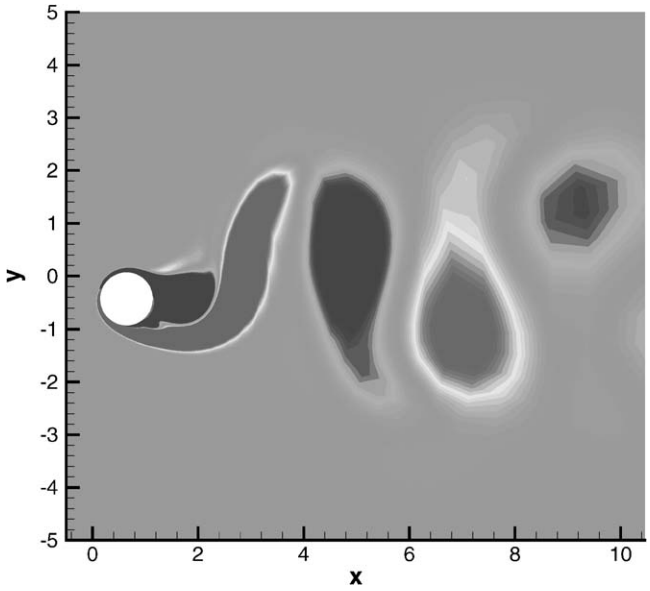

Fig. 7. Vorticity contours around the oscillating cylinder, $\mu_s = 1.2732$, $\zeta = 0.03166$.

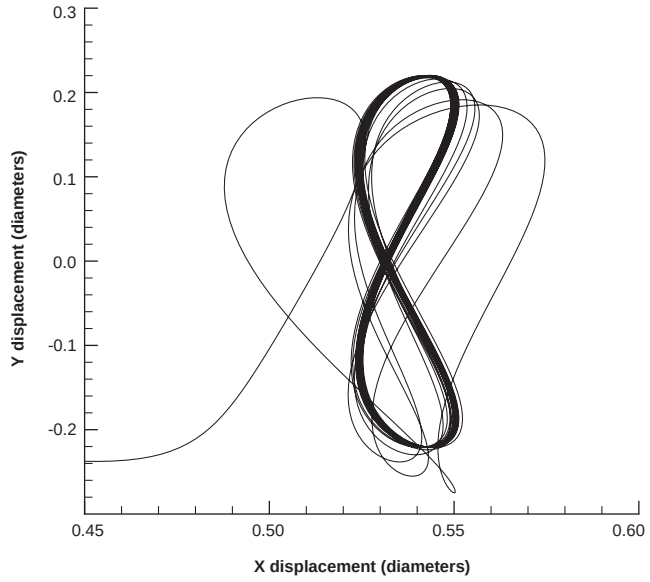

Fig. 8. The trajectory of the center position of the oscillating cylinder, $\mu_s = 1.2732$, $\zeta = 0.63326$.

Morton et al. (1997) are $M = 0.1$ and $\mathrm{Re} = 200$, which are different from those used by Alonso et al. (1995) and the authors ($M = 0.2$ and $\mathrm{Re} = 500$).

5.2. Elastically mounted airfoil

5.2.1. Steady state transonic airfoil

As validation for the Zha–Hu CUSP scheme for transonic airfoils, the steady-state solution of the transonic RAE 2822 airfoil is calculated first. The freestream conditions for this study are listed in Table 2.

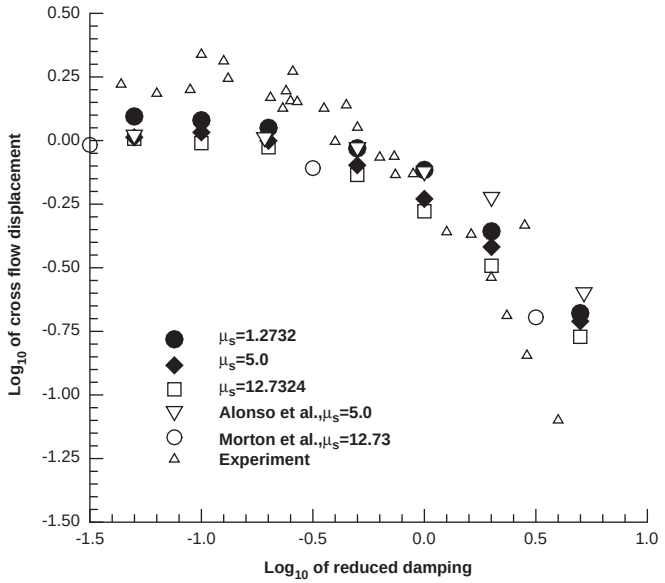

Fig. 9. Comparison of the computed amplitude with Griffin's (1992) experimental data for the elastically mounted cylinder.

Table 2
Free-stream conditions for RAE 2822 airfoil

Mach	Static pressure (psia)	Temperature (R)	Angle-of-attack (deg)	Re
0.729	15.8073	460.0	2.31	6.5×10^6

The turbulent Reynolds stress and heat flux are calculated by the Baldwin–Lomax algebraic model (Baldwin and Lomax, 1978). This case is run using an O-type grid with three different dimensions, which are $128 \times 50 \times 1$, $256 \times 55 \times 1$, and $512 \times 95 \times 1$, respectively.

Numerical experiments are conducted to determine the far-field boundary. The far-field boundary distance of 15 chords is chosen because the numerical solution does not change any more if the far field boundary is moved away further. The far-field boundary is not determined to specially favor a particular aerodynamic parameter such as lift or drag.

The experimental data provided by Cook et al. (1979) are available for validation. The comparison of pressure coefficients on the airfoil is shown in Fig. 10. Overall, very good agreement is obtained between the computation and experiment for each mesh dimension, especially for the two larger ones which appear to sufficiently capture the shock on the suction surface of the airfoil without using any limiter. The important aerodynamic coefficients from both simulation and experiment are summarized in Table 3.

It can be seen in Table 3 that the predicted lift coefficients with all mesh dimensions agree well with experiment. The computed drag and moment coefficients show larger errors, but they have the similar accuracy as those computed by Prananta et al. (1998). The relatively large errors of the drag and moment may be mostly due to the inadequacy of the turbulence model. The experimental wind tunnel set-up causing the boundary condition mismatch between the CFD and experiment may also have some contribution.

5.2.2. Forced pitching airfoil

As a validation case of the scheme for a moving grid system, the forced pitching NACA 64A010 airfoil is calculated. For this transonic airfoil, the Reynolds averaged Navier–Stokes equations with Baldwin–Lomax turbulence model are solved. Similar to the previous computation of the flow over the stationary airfoil, an O-type mesh consisting of

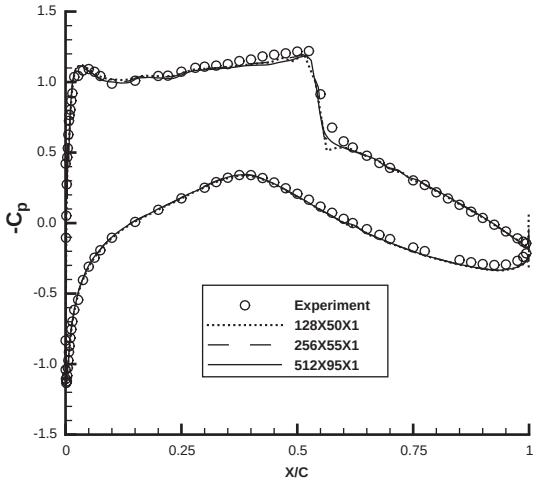

Fig. 10. Surface pressure coefficient comparison for RAE 2822 airfoil at $M = 0.729$.

Table 3
Aerodynamic coefficients and $y+$ for RAE 2822 airfoil

Mesh dimension	C_d	C_l	C_m	$y+$
128×50	0.01482	0.73991	0.09914	0.0833–2.3864
256×55	0.01455	0.73729	0.09840	0.1318–2.4016
512×95	0.01426	0.74791	0.09994	0.2309–2.0228
Prananta et al. (1998)	0.01500	0.74800	0.09800	
Experiment	0.01270	0.74300	0.09500	

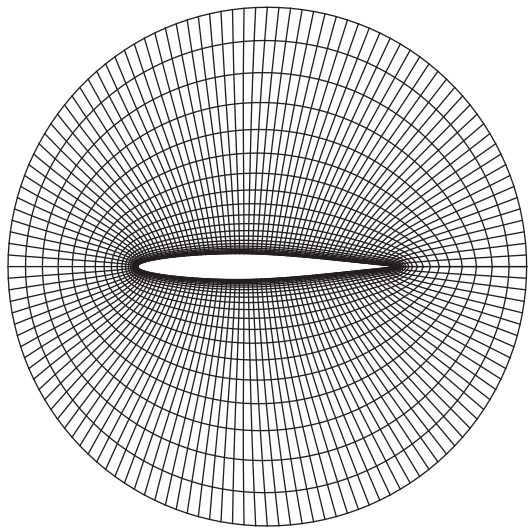

Fig. 11. The near wall O-type mesh around the NACA 64A010 airfoil.

280×65 cells is employed for the computations of forced pitching airfoil. The NACA 64A0101 airfoil is selected for this calculation due to the availability of experimental data. The fine mesh zone for the non-deforming part of the mesh is shown in Fig. 11. The first grid point adjacent to the wall has the maximum $y^+ \leqslant 3.43$.

The NACA 64A0101 airfoil is forced in pitch around its quarter chord sinusoidally. The angle of attack is imposed as a function of time, $\alpha(t) = \alpha_m + \alpha_o \sin(\omega t)$, where α_m and α_o are the mean angle of attack and the amplitude of oscillation, respectively. The ω is the angular frequency, which is directly related to the reduced frequency $k = \omega c/2U_\infty$, where c is the airfoil chord and U_∞ is the free-stream velocity. To compare with the experimental results given by Davis (1982), the primary parameters used in the computation are listed as follows: $\alpha_m = 0,\ \alpha_o = 1.01^\circ,\ \mathrm{Re} = 1.256 \times 10^7,\ M_\infty = 0.8,\ k = 0.202$.

Again, the computation begins with the steady-state flow field of the stationary airfoil at 0° angle of attack with a dimensionless time step $\Delta t = 0.1$. Convergence for each time step is reached when the maximum residual of the CFD solver is decreased by 3–4 orders of magnitude or the solution is marched in pseudo time until 100 iterations. The transient period takes about 3 cycles, and the result becomes periodic in time after that. Fig. 12 shows the lift oscillation versus the angle of attack after the flow field reaches its temporally periodic solution. The computed lift oscillation agrees well with the experiment (Davis, 1982).

Fig. 13 shows the computed moment coefficient compared with experiment (Davis, 1982). The computed moment coefficient does not agree as accurately with the experiment as the lift coefficient does. However, the results are very similar to those predicted by Bohbot and Darracq (2001) and McMullen et al. (2002). The large discrepancy between computation and the experiment for the moment coefficient may be due to the inadequacy of the turbulence modeling and experimental uncertainties.

The mean pressure coefficients, or zero harmonic of pressure coefficient, on the airfoil surface are shown in Fig. 14. The numerical results show a fairly good agreement with the experimental data. Fig. 15 shows the instantaneous pressure coefficients on the airfoil surface at various angles of attack. The numerical and experimental data are recorded as the airfoil pitches down from its extreme position value of 1° to its negative extreme value of -1°. The comparisons between the numerical and experimental results show that the computed pressure coefficients upstream of the shock are slightly under predicted. The weak shock position and strength, and the overall surface pressure coefficients are accurately predicted by the computation. The good agreement of the surface pressure with the experiment indicates again that the moment deviation from experiment may be mostly due to the surface skin friction prediction, which is mainly determined by the turbulence modeling.

5.3. Free vibration of NACA 64A010 in transonic flow

The structural model for the 2-D airfoil made from a 3-D sweptback wing with a NACA 64A010 cross-section is described in Section 3.2. This model was first introduced by Isogai (1981), and has been numerically investigated by

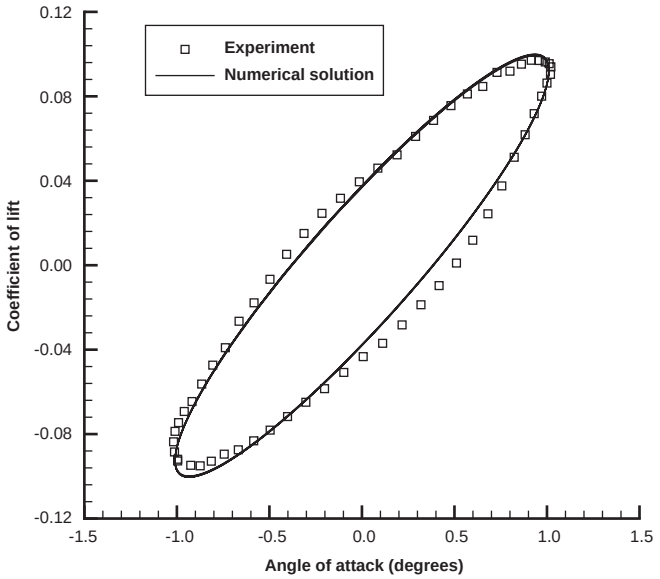

Fig. 12. Comparison of computed lift coefficient with Davis' (1982) experimental data for the forced pitching airfoil.

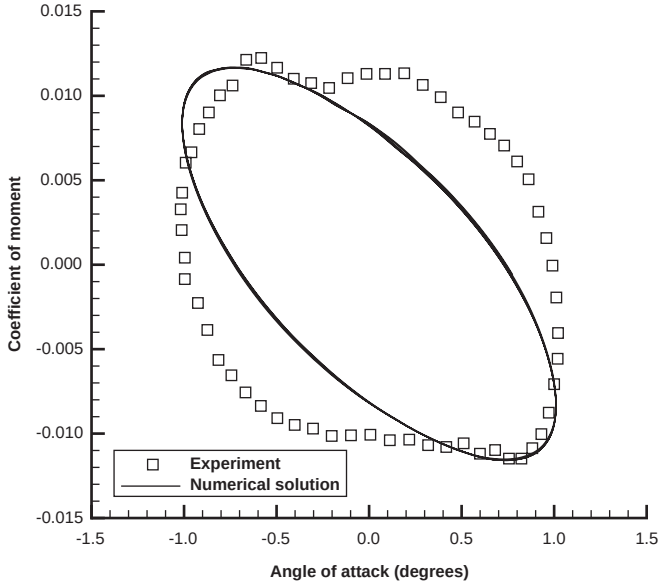

Fig. 13. Comparison of computed moment coefficient with Davis' (1982) experimental data for the forced pitching airfoil.

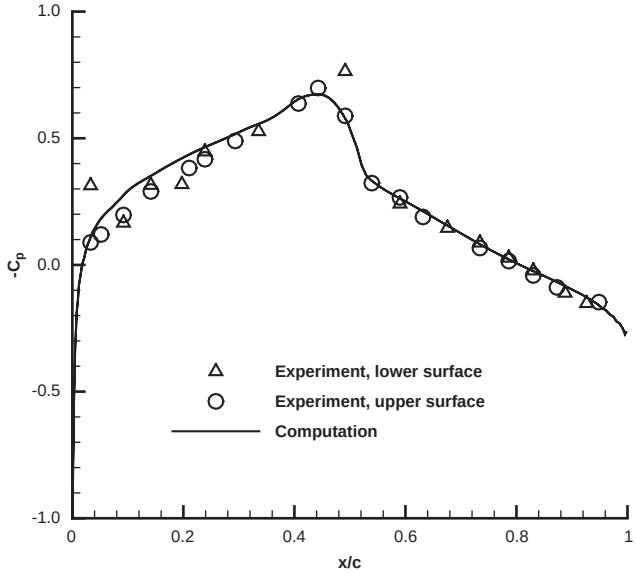

Fig. 14. Comparison of the mean pressure distribution along the pitching airfoil.

several researchers (Bendiksen and Kousen, 1987; Alonso and Jameson, 1994; Prananta et al., 1998; Bohbot and Darracq, 2001), whose work and numerical results are used as comparison references for the present study. The structural parameters used in this model are as follows: $a = -2.0$, $x_\alpha = 1.8$, $\omega_\alpha/\omega_h = 1$, $r_\alpha^2 = 3.48$, and $\mu = 60$. The elastic axis is located half a chord upstream of the airfoil leading edge.

The unsteady Reynolds averaged Navier–Stokes equations with the Baldwin–Lomax turbulence model are solved for the flow field in this study. The freestream conditions are: $\mathrm{Re} = 1.256 \times 10^7$, $M_\infty = 0.825$.

Due to the symmetric profile of the NACA 64A010 airfoil, an initial perturbation is imposed to trigger the oscillating motion. The airfoil is forced to rotate sinusoidally about its elastic axis at the natural frequency in pitch ω_α, with an angle of attack amplitude, $\alpha_o = 1^\circ$. Usually the forced pitching mode lasts for 1–3 cycles. After that, the elastically mounted airfoil is allowed to move in both plunging and pitching directions, and then the dynamic

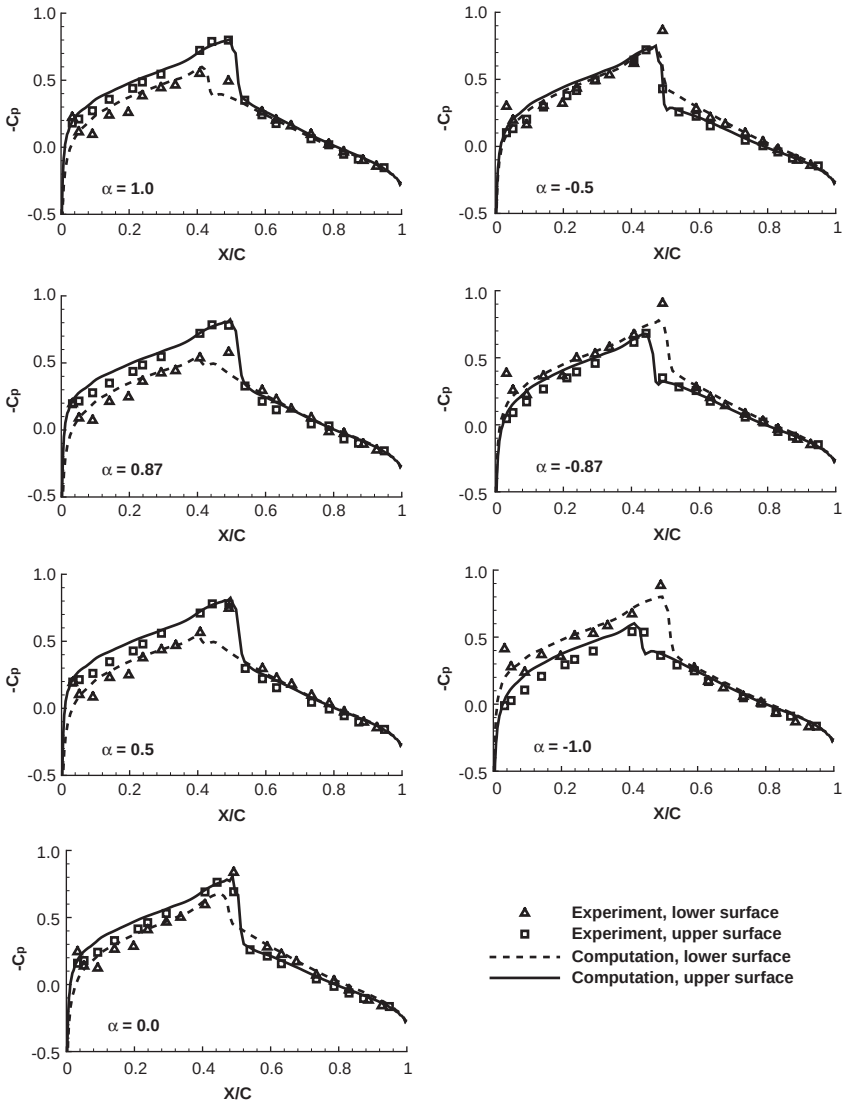

Fig. 15. Comparison of the instantaneous pressure distributions at various angles of attack.

response is recorded. During each time step, the CFD and the structural equations are solved until both residuals of CFD and structural solvers are at least reduced by 3–4 orders of magnitude or the number of pseudo time steps reaches 100.

In the present study, the search of the critical point on the transonic flutter boundary at a given Mach number is conducted. The speed index, V^* defined as $U^*/\sqrt{\mu}$, is the parameter to classify damped, neutral and divergent responses of the airfoil when the Mach number is fixed. In this case, the total pressure and temperature need to be adjusted to match the certain value of the Reynolds number. Several calculations are needed to determine the critical point using a bi-section method.

In Figs. 16–18 the time histories of plunging and pitching displacements at $M_\infty = 0.825$ are plotted for three different V^*. In these figures, from $V^* = 0.55$ to 0.70, the plots correspond to the damped, neutral, and diverging responses, respectively. The major task of calculating a flutter boundary is to locate where the neutrally stable, or critical point, is by looking at those plots and determining where the neutral response occurs as V^* varies. When the value of V^* is smaller than the critical value on the flutter boundary, both plunging and pitching displacements decay corresponding to the damped response as shown in Fig. 16. Once the value of V^* coincides with or is close to the critical value, the neutral response appears as shown in Fig. 17. For a value of V^* beyond the critical value, a diverging response is

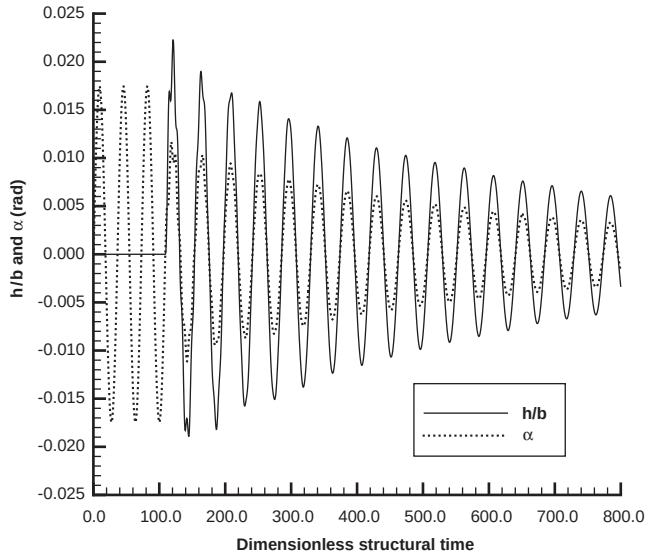

Fig. 16. Time histories of plunging and pitching displacements for $M_\infty = 0.825$ and $V^* = 0.55$; damped response.

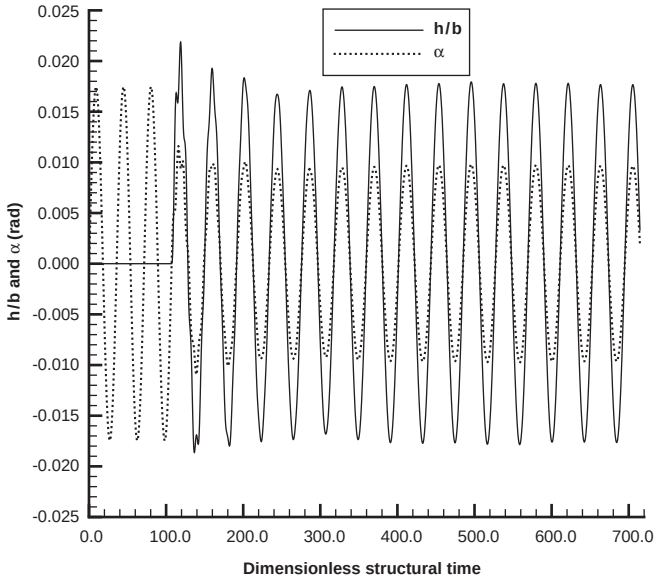

Fig. 17. Time histories of plunging and pitching displacements for $M_\infty = 0.825$ and $V^* = 0.615$; neutrally stable response.

expected as shown in Fig. 18. The bottom of the sonic dip is located at Mach = 0.825 as reported in Chen et al. (2004), Prananta et al. (1998), Bohbot and Darracq (2001). The predicted critical velocity index $V^* = 0.615$ is consistent with the results computed by those researchers.

6. Conclusion

The efficient high-resolution E-CUSP upwind scheme newly suggested by Zha and Hu (2004) has been successfully extended and applied to calculate flow-induced vibration with a moving grid based on fully coupled fluid–structural interaction.

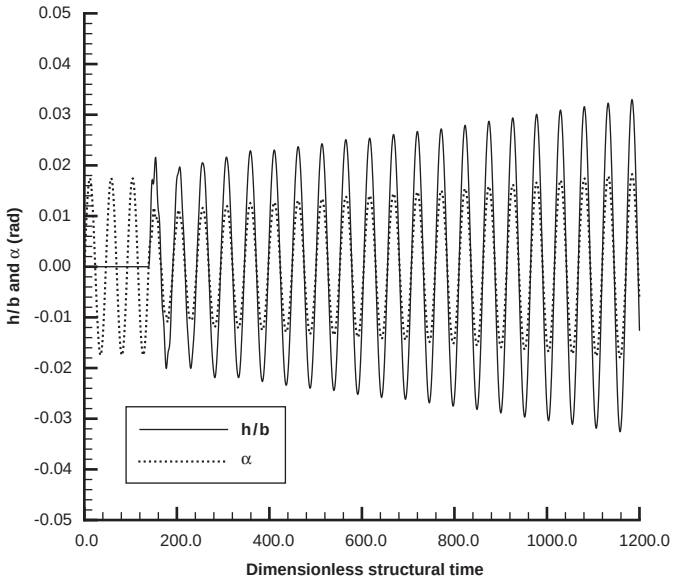

Fig. 18. Time histories of plunging and pitching displacements for $M_\infty = 0.825$ and $V^* = 0.70$; diverging response.

For an elastically mounted cylinder, various cases with different structural parameters have been calculated. The predicted displacement agrees very well with experiment and numerical results of other researchers.

For the forced pitching NACA 64A010 airfoil, the computed lift oscillation agrees accurately with the experiment. The computed moment oscillation has large deviations from the experiment at ones, but the results have a similar order of accuracy as other researchers have achieved numerically. The discrepancy may be due to the inaccurate prediction of the surface shear stress caused by the inadequacy of the turbulence modeling and experimental uncertainties.

The same airfoil has been used in calculations of an elastically mounted airfoil with free vibration in the plunging and pitching directions. The computations have been carried out using different values of the velocity index V^* which are below, close, and beyond the critical point on the flutter boundary when the Mach number is fixed. The corresponding responses about the flows are well simulated. The predicted value of V^* at the bottom of the transonic dip is consistent with the numerical results of other researchers (Chen et al., 2004; Bohbot and Darracq, 2001; Prananta et al., 1998).

The E-CUSP scheme of Zha–Hu has been proved to be robust, accurate and efficient for calculating flow-induced vibrations based on fully coupled fluid–structural interaction.

Acknowledgements

This work is supported by AFOSR Grant F49620-03-1-0253 monitored by Dr Fariba Fahroo, Major William Hilbun, and Dr. Dean Mook.

References

Alonso, J.J., Jameson, A., 1994. Fully-implicit time-marching aeroelastic solutions. AIAA Paper 94-0056.

Alonso, J.J., Martinelli, L., Jameson, A., 1995. Multigrid unsteady Navier–Stokes calculations with aeroelastic applications. AIAA Paper 95-0048.

Baldwin, B.S., Lomax, H., 1978. Thin-layer approximation and algebraic model for separated turbulent flows. AIAA Paper 78-257.

Bendiksen, O.O., Kousen, K.A., 1987. Transonic flutter analysis using the Euler equations. AIAA Paper 87-0911.

Blackburn, H.M., Karniadakis, G.E., 1993. Two and three-dimensional vortex-induced vibration of a circular cylinder. ISOPE-93 Conference, Singapore.

Blom, F.J., Leyland, P., 1997. Analysis of fluid–structure interaction by means of dynamic unstructured meshes. AD-Vol. 53-3, Fourth International Symposium on Fluid–Structure Interaction, Aeroelasticity, Flow-Induced Vibrations and Noise, vol. I, ASME.

Bohbot, J., Darracq, D., 2001. Time domain analysis of two D.O.F. airfoil flutter using an Euler/turbulent Navier–Stokes implicit solver. International Forum on Aeroelasticity and Structural Dynamics, Madrid, Spain, June 5–7.

Chen, X.-Y., Zha, G.-C., Hu, Z.-J., 2004. Numerical simulation of flow induced vibration based on fully coupled-structural interactions. AIAA Paper 2004-2240.

Cook, P.H., McDonald, M.A., Firmin, M.C.P., 1979. Aerofoil RAE 2822-Pressure distributions, and boundary layer and wake measurements. Experimental data base for computer program assessment. AGARD Report AR-138.

Darracq, S., Champagneux, S., Corjon, A., 1998. Computation of unsteady turbulent airfoil flows with an aeroelastic AUSM+ implicit solver. AIAA Paper 98-2411.

Davis, S.S., 1982. NACA 64 A010 (NACA Ames model) oscillatory pitching. AGARD Report No. 702.

Edwards, J.R., 1995. A low-diffusion flux-splitting scheme for Navier–Stokes calculations. AIAA Paper 95-1703-CP.

Edwards, J.R., 1997. A low-diffusion flux-splitting scheme for Navier–Stokes calculations. Computer & Fluids 6, 635–659.

Giles, M.B., 1995. Stability and accuracy of numerical boundary conditions in aeroelastic analysis. Report No. 95/13, Oxford University Computing Laboratory.

Goldstein, S., 1938. Modern Developments in Fluid Dynamics. Clarendon Press, Oxford.

Griffin, O.M., 1992. Vortex-induced vibrations of marine structures in uniform and sheared currents. NSF Workshop on Riser Dynamics, University of Michigan.

Guruswamy, G.P., 1990. Unsteady aerodynamic and aeroelastic calculations for wings using Euler equations. AIAA Journal 28, 461–469.

Hänel, D., Schwane, R., Seider, G., 1987. On the accuracy of upwind schemes for the solution of the Navier–Stokes eqautions. AIAA paper 87-1105-CP.

Isogai, K., 1981. Transonic dip mechanism of flutter of a sweptback wing: part II. AIAA Journal 19, 1240–1242.

Jameson, A., 1991. Time dependent calculations using multigrid with application to unsteady flows past airfoils and wings. AIAA Paper 91-1596.

Jameson, A., 1993. Analysis and design of numerical schemes for gas dynamics I: artificial diffusion, upwind biasing, limiters and their effect on accuracy and multigrid convergence in transonic and hypersonic flow. AIAA Paper 93-3359.

Jameson, A., 1995a. Analysis and design of numerical schemes for gas dynamics I: artificial diffusion, upwind biasing, limiters and their effect on accuracy and multigrid convergence in transonic and hypersonic flow. Journal of Computational Fluid Dynamics 4, 171–218.

Jameson, A., 1995b. Analysis and design of numerical schemes for gas dynamics II: artificial diffusion and discrete shock structure. Journal of Computational Fluid Dynamics 5, 1–38.

Lee-Rausch, E.M., Batina, J.T., 1996. Wing flutter computations using an aerodynamics model based on the Navier–Stokes equations. Journal of Aircraft 33, 1139–1147.

Liou, M.-S., 1996. A sequel to AUSM: AUSM^{+}. Journal of Computational Physics 129, 364–382.

Liu, F., Cai, J., Zhu, Y., Wong, A.S.F., Tsai, H.M., 2000. Calculation of wing flutter by a coupled CFD-CSD method. AIAA 2000-0907.

McMullen, M., Jameson, A., Alonso, J., 2002. Application of a non-linear frequency domain solver to the Euler and Navier–Stokes equations. AIAA Paper 2002-0120.

Melville, R.B., Morton, S.A., 1998. Fully implicit aeroelasticity on overset grid systems. AIAA Paper 98-0521.

Melville, R.B., Morton, S.A., Rizzetta, D.P., 1997. Implementation of a fully-implicit, aeroelastic Navier–Stokes solver. AIAA Paper 97-2039.

Morton, S.A., Melville, R.B., Visbal, M.R., 1997. Accuracy and coupling issues of aeroelastic Navier–Stokes solutions on deforming meshes. AIAA Paper 97-1085.

Prananta, B.B., Hounjet, M.H.L., Zwaan, R.J., 1998. Two-dimensional transonic aeroelastic analysis using thin-layer Navier–Stokes method. Journal of Fluid and Structures 12, 655–676.

Roshko, A., 1954. On the development of turbulent wakes from vortex streets. NACA Report No. 1191.

Smith, M.J., 1989. Flight loads prediction methods for aircraft: vol. I. Euler/Navier–Stokes aeroelastic method (ENS3DAE) technical development summary: Version 4.0. WRDC-TR-89-3104.

Thomas, P.D., Lombard, C.K., 1979. Geometric conservation law and its application to flow computations on moving grids. AIAA Journal 17, 1030–1037.

Vermeersch, S.A., Raj, P., Weed, R.A., Sankar, L.N., 1997. Towards cost-effective aeroelastic analysis on advanced parallel computing systems. AIAA Paper 97-0646.

Zha, G.-C., 2004. A low diffusion E-CUSP upwind scheme for transonic flows. AIAA Paper 2004-2707.

Zha, G.-C., Hu, Z.-J., 2004. Calculation of transonic internal flows using an efficient high resolution upwind scheme. AIAA Journal 42, 205–214.